Realistic Fröhlich Scattering and Mobility of 2D Semiconductors

in van der Waals Heterostructure

Chenmu Zhang, Yuanyue Liu[*]

Texas Materials Institute and Department of Mechanical Engineering,

The University of Texas at Austin, Austin, Texas 78712, USA

Yuanyue.liu@austin.utexas.edu

Abstract:

Two-dimensional (2D) semiconductors have demonstrated great potential for next-generation electronics and optoelectronics. Their atomic thinness facilitates the material design for desirable electronic properties when combined with other 2D materials in van der Waals (vdW) heterostructure. Although the carrier mobility has been well studied for suspended 2D semiconductors via first-principles calculation recently, it is not clear how they are affected by surrounding materials. In this work, we propose a model to consider the Fröhlich scattering, an important scattering in polar materials from polar-optical (PO) phonons, in vdW heterostructures. Exemplified by InSe surrounded by h-BN, we found the InSe Fröhlich mobility can be enhanced about 2.5 times by environmental dielectric screening and coupled PO phonons in vdW heterostructures. More interestingly, the strong remote PO phonons can enhance the InSe mobility instead of deteriorating it once considering the PO phonons coupling. Then several quantities of surrounding dielectrics are proposed to optimize the InSe Fröhlich mobility, and then used for filtering potential 2D dielectric materials. Our work provides efficient calculation tools as well as physical insights for carrier transport of 2D semiconductors in realistic vdW heterostructures.

Introduction:

Two-dimensional (2D) semiconductors are layered semiconducting materials with a thickness of only one or few atomic layer(s), weakly bounded to neighboring layers due to their dangling-bond-free surfaces. When stacked with various other 2D materials via van der Waals (vdW) interactions, the vdW heterostructures can be built without the constraints of lattice matching and processing compatibility for individual layers. It offers unprecedented opportunities for properties tuning, such as band gap engineering, twistronics, plasmonics and so on [1-3]. One of the useful properties is the carrier mobility. The current 2D semiconductors suffer from relatively poor carrier transport properties at room temperature [4]. For example, the upper limit of intrinsic carrier mobility (ignoring impurity scatterings) of MoS_2 monolayer is predicted < 200 $cm^2V^{-1}s^{-1}$ based on various first-principles calculations [5-7]. Many 2D semiconductors, including many 2D transition metal dichalcogenides [8] and indium selenide (InSe) [5,9] suffer from strong Fröhlich scattering induced by polar-optical phonons (POPs). Although many studies have been carried out on transport properties of 2D semiconductor, most of calculations focus on suspended monolayers, which is far from the realistic operation regime and ignores the effects of surrounding layers. It is still elusive how will the carrier mobility of 2D semiconductor change in different vdW heterostructures.

For non-vdW heterostructures, the dielectric continuum model [10-12] is proposed to compute the remote phonon scattering rates. By assuming the semiconductors as dielectric continuum, an analytical equation for remote phonon scattering rates can be obtained. However the complexity of the equations grows with the number of heterointerfaces in the system, and usually single- or double heterointerface systems are studied. Therefore, only simple heterostructures like double heterojunctions [13-16] or 2D materials embedded in semi-infinite substrates [17-22] are studied in the past. In addition to the complexity in vdW dielectrics, the dielectric continuum model takes materials as continuum and neglects the atomic details, which is important for atomically thin 2D semiconductors. For example, the confined phonon wavelength in model might be lower than the thickness of 2D semiconductor and lead to fictitious electron-phonon scattering [10]. In addition, the POPs coupling between the 2D semiconductor and dielectrics are usually neglected [22], which, as we will see in the following, leads to considerable errors on scattering rates and mobility calculations.

In this work, we propose a simple and efficient model to consider Fröhlich scattering and mobility in channel materials in vdW heterostructures. The effects of surrounding layers can be mainly divided into two parts: First, the electrons in surrounding materials provide dielectric screening for the electrostatic field generated by POPs, which alleviates the Fröhlich scattering and thus increases the mobility. Second, the POPs contributed from surrounding dielectrics influence the electrons as well as the POPs in the channel material, and consequently affect the mobility in a nontrivial fashion. We found the overall effect of these remote PO phonons will significantly enhance the mobility in 2D semiconductors in most cases, which contradicts the intuitive that the remote phonon scattering usually reduces the mobility. Exemplified by InSe surrounded by h-BN layers, we shown that the InSe Fröhlich mobility can be enhanced about 2.5 times by environmental dielectric screening and coupled POPs in vdW heterostructures. The InSe mobility can be further improved once the surrounding materials satisfying more desirable properties, i.e. moderate POP frequency, large Born effective charge and smaller in-plane polarizability. Using these descriptors, we filtered additional potential dielectrics besides h-BN from 2D materials database for optimal intrinsic InSe mobility. The discovered dielectric materials as well as the mechanistic insights shed light on vdW heterostructure design for next-generation electronics/optoelectronics.

Methods:

The carrier mobility μ for band transport at low electric field can be obtained from the Boltzmann transport theory under momentum relaxation time approximation [5,6]:

$$\mu_{\alpha\beta} = \frac{q}{n_c A} \sum_n \int \frac{d\mathbf{k}}{A_{\text{BZ}}} \frac{\partial f_{n\mathbf{k}}}{\partial E_{n\mathbf{k}}} \tau_{n\mathbf{k}} v_{n\mathbf{k},\alpha} v_{n\mathbf{k},\beta}, \tag{1}$$

where α and β are the direction indices, q is the charge of carrier, A (A_{BZ}) is the area of unit cell (Brillouin zone); $\tau_{n\mathbf{k}}$ is the momentum relaxation time for the electronic state with band index n and wavevector $\mathbf{k}$, $v_{n\mathbf{k}}$ is its group velocity, and $E_{n\mathbf{k}}$ is its energy; f is the Fermi distribution function, and n_c is the carrier density which is related with f and the electronic band structure through:

$$n_e = \sum_n \int \frac{d\mathbf{k}}{A_{\text{BZ}}} f_{n\mathbf{k}}; \quad n_h = \sum_n \int \frac{d\mathbf{k}}{A_{\text{BZ}}} (1 - f_{n\mathbf{k}}), \tag{2}$$

where n_e and n_h are the concentrations for electrons and holes respectively. Since we are interested in the Fröhlich-limited mobility, we consider a perfect material with the Fermi level at the middle of the band gap and the Fröhlich scattering only. The Fröhlich-limited relaxation τ^F can be calculated as:

$$\frac{1}{\tau_{n\mathbf{k}}^F} = \frac{2\pi}{\hbar} \sum_{mv} \int_{BZ} \frac{d\mathbf{q}}{A_{BZ}} | \bar{g}_{mnv}^F(\mathbf{k},\mathbf{q})|^2 [(f_{m\mathbf{k}+\mathbf{q}} + n_{v\mathbf{q}})\delta(E_{n\mathbf{k}} - E_{m\mathbf{k}+\mathbf{q}} + \hbar\omega_{v\mathbf{q}})$$
$$+ (1 + n_{v\mathbf{q}} - f_{m\mathbf{k}+\mathbf{q}})\delta(E_{n\mathbf{k}} - E_{m\mathbf{k}+\mathbf{q}} - \hbar\omega_{v\mathbf{q}})](1 - \frac{\mathbf{v}_{n\mathbf{k}} \cdot \mathbf{v}_{m\mathbf{k}+\mathbf{q}}}{|\mathbf{v}_{n\mathbf{k}}||\mathbf{v}_{m\mathbf{k}+\mathbf{q}}|}), \tag{3}$$

where the initial electronic state $n\mathbf{k}$ is scattered to the final state $m\mathbf{k}+\mathbf{q}$ by interacting with a phonon $v\mathbf{q}$ with frequency $\omega_{v\mathbf{q}}$ (v is the phonon band index and $\mathbf{q}$ is the phonon wavevector); n is the Bose distribution; $\mathbf{v}$ is the group velocity vector; g^F is the Fröhlich coupling (EPC) matrix element. In suspended monolayer case, the g^F induced by phonon $v\mathbf{q}$ can be obtained by:

$$g_v^F(\mathbf{k},\mathbf{q}) = \frac{ie^2}{2A} \sum_{\alpha,i} \left(\frac{\hbar}{2M_\alpha \omega_{v\mathbf{q}}}\right)^{1/2} \frac{(\mathbf{q} \cdot \mathbf{Z}_\alpha^*)_i e_{v;\alpha i}(\mathbf{q})}{q \varepsilon^{\parallel}(\mathbf{q})} \langle \psi_{\mathbf{k}+\mathbf{q}} | e^{i\mathbf{q} \cdot (\mathbf{r} - \tau_\alpha)} | \psi_{\mathbf{k}} \rangle \tag{4}$$

where α is the index of the atom in the unit cell, M is the atomic mass, $\mathbf{Z}^*$ is the Born effective charge, τ_α is the atomic position in the unit cell; $\varepsilon^{\parallel}$ is the in-plane dielectric function of the 2D material, ψ is the wavefunction of initial or final electronic state; i is the cartesian index, $e_v(\mathbf{q})$ is the phonon eigenvector describing how much the α-th atom moves in the i direction in phonon $v\mathbf{q}$. Here we ignore the band index m, n for simplicity and $\langle \psi_{\mathbf{k}+\mathbf{q}} | e^{i\mathbf{q} \cdot (\mathbf{r} - \tau_\alpha)} | \psi_{\mathbf{k}} \rangle$ can be approximated by 1 since the Fröhlich scattering involves phonon with small $|\mathbf{q}|$.

The Eq. 4, widely used in 2D semiconductor mobility calculations, is only valid for suspended monolayer. When stacked with surrounding layers, the semiconductor's g^F will be affected by vdW heterostructures mainly in 3 aspects: (1) The in-plane dielectric function $\varepsilon^{\parallel}$ of the channel materials will be increased due to the environmental dielectric screening from surrounding layers, as shown in Fig. 1a. The larger $\varepsilon^{\parallel}$ will lead to smaller g^F, larger relaxation τ^F and thus larger Fröhlich mobility μ^F. (2) As shown in Fig. 1b, the remote POPs (here we refer the POPs to the $\mathbf{q} \cdot \mathbf{Z} \cdot \mathbf{e} \neq 0$ components from all phonon eigenvectors) will also scatter the electrons in the channel material, leading to v insufficient to describe all POPs existing in the vdW heterostructure. Therefore, it is necessary to use a larger phonon band index μ for whole vdW heterostructure (or equivalently lv representing v-th phonon mode in l-th layer) to include the additional g^F induced by these remote POPs. (3) The remote phonons will be coupled with the phonons from the channel material, which will modify the phonon eigenvector $e_\mu(\mathbf{q})$ and thus the g^F. In this work (Fig. 1c), we consider the POP coupling due to the long-range electrostatic potential induced by corresponding POP vibrations. To evaluate the realistic $e_\mu(\mathbf{q})$ in the vdW heterostructure, it will be necessary to build up a dynamical matrix D for whole vdW heterostructure and then calculate the eigen-vibrations by diagonalization of D. In the following, we start from deriving the D of whole vdW heterostructure and then evaluate the g^F based on approximations on D. With g^F in hand, we insert it into Eq. 3 and use Eq. 1 to compute the Fröhlich mobility in vdW heterostructure.
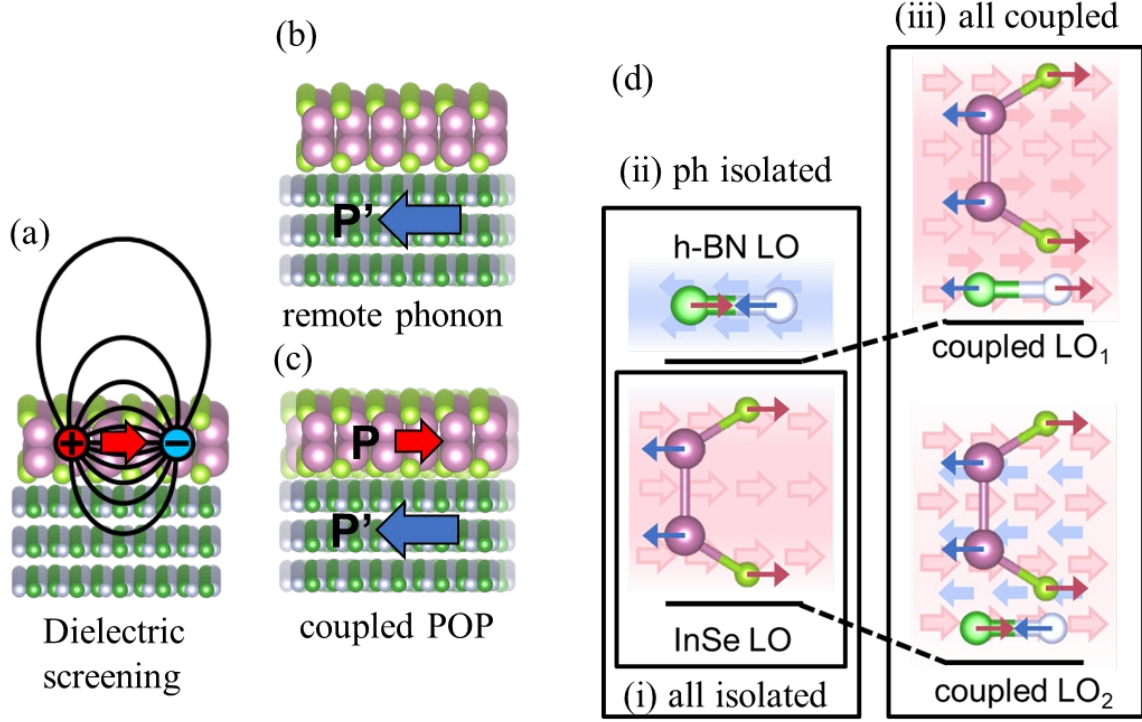
Figure 1. Diagrams of three different effects of surrounding layers in vdW heterostructure on carrier transport of top channel materials: (a) dielectric screening, (b) remote phonon scattering and (c) POP coupling. (d) The diagram of POP coupling exemplified by InSe and h-BN bilayers. The blur arrows in the background indicates the electrostatic field induced by POP vibrations, and the thick arrows connected to atoms indicates the POP vibrations. The left (right) column represents POPs without (with) coupling.

The dynamical matrix D for phonons in vdW heterostructures (see Appendix A for derivations) can be divided into analytic contribution D^a and nonanalytic contribution D^{na} [23]:

$$D_{l\alpha i,l'\alpha'i'}(\mathbf{q}) = D^a_{l\alpha i,l'\alpha'i'}(\mathbf{q}) + D^{na}_{l\alpha i,l'\alpha'i'}(\mathbf{q})$$

$$= D^a_{l\alpha i,l'\alpha'i'}(\mathbf{q}) + e^2 z_{l\alpha i} z^*_{l'\alpha'i'} \frac{|\mathbf{q}|^2 \bar{W}_{ll'}(\mathbf{q})}{\sqrt{A_l A_{l'}}} \qquad (5)$$

where $\bar{W}_{ll'}$ is the screened Coulomb interaction (See Appendix B for details) between l and l' layers, $z_{l\alpha i}$ is effective Born effective charge corresponding to atom α in l layer moving i direction: $z_{l\alpha i} = (\hat{\mathbf{q}} \cdot \mathbf{Z}^*_{l\alpha})_i / \sqrt{M_{l\alpha}}$. Since we are interested in Fröhlich scattering which involves intravalley scattering with small $|\mathbf{q}|$, the $D^a(\mathbf{q})$ is approximated by its value around $\mathbf{q}=0$. Furthermore, the interlayer coupling in D^a is neglected, so the D^a in Eq. 5 can be calculated via density functional perturbation theory (DFPT) for individual layers in vdW heterostructure at single $\mathbf{q}$ point ($\mathbf{q} \rightarrow 0$):

$$D^a_{l\alpha i,l'\alpha'i'} = \sum_l \delta_{ll'} D^a_{l\alpha i,l\alpha'i'}(\mathbf{q} \rightarrow 0) \qquad (6)$$

The dimension of D in Eq. 5 is linear with the number of layers in the vdW heterostructure, leading

to difficulty in matrix diagonalization. Therefore, we first diagonalize the D^a and use the eigenvectors of D^a as the basis of D. The new eigenvector basis $e_{\mathbf{q}lv}$ can be easily obtained by diagonalization of D^a for individual layers. Under this new basis, the D in Eq. 5 can be written as:

$$D_{lv,l'v'}(\mathbf{q}) = \delta_{ll'}\delta_{vv'}\omega_{0lv}^2 + e^2 z_{lv} z_{l'v'}^* \frac{|\mathbf{q}|^2 \overline{W}_{ll'}(\mathbf{q})}{\sqrt{A_l A_{l'}}} \tag{7}$$

where ω_{0lv} is the phonon frequency at $\mathbf{q}=0$ for v mode in l layer, z_{lv} is the effective Born effective charges from collective atom displacement:

$$z_{lv} = \sum_{\alpha i} \frac{(\hat{\mathbf{q}} \cdot \mathbf{Z}_{l\alpha}^*)_i e_{\mathbf{q}lv;\alpha i}}{\sqrt{M_{l\alpha}}} \tag{8}$$

The D in Eq. 7 has many zero elements and can be calculated as a sparse matrix, which facilitates the diagonalization. The diagonalization of D in Eq. 7 generates a set of eigenvectors $\tilde{e}_{\mathbf{q}\mu}$ and the eigenvalues $\tilde{\omega}_{\mathbf{q}\mu}^2$, where μ is the phonon band index in the whole vdW heterostructure. The Fröhlich matrix element (see Appendix A for derivations) for electrons in l layer due phonon $\mu\mathbf{q}$ is:

$$g_{l\mu}^{\mathrm{F}}(\mathbf{k},\mathbf{q}) = \sum_{l'v} \frac{-i}{\sqrt{A_l A_{l'}}} \frac{w_{q\mu;l'v}}{\sqrt{2\tilde{\omega}_{\mathbf{q}\mu}}} |\mathbf{q}| W_{l'l}(\mathbf{q}) z_{l'v} \tag{9}$$

The $W_{l'l}$ is the screened potential in l layer induced by charge from l' layer, which can be calculated from Quantum Electrostatic Heterostructure (QEH) model [24,25] (see Appendix B for details). Inserting g^{F} from Eq. 9 into Eq. 3 will give Fröhlich relaxation time τ^{F}, and with τ^{F} we can calculate the Fröhlich mobility μ^{F} using Eq. 1.

Results and discussion:

Before discussing the consequent μ^{F}, we use different levels of approximation and try to isolate the different effects of surrounding layers. Here we use InSe/BN vdW heterostructure as an example, consisting of InSe monolayer and multilayer h-BN. The h-BN can be located on both sides or only one side of the InSe. The layer index of InSe is fixed as 0. The first approach stresses the importance of dielectric screening and is called "all isolated" as shown in diagram in Fig. 2d. It neglects all the remote phonons in the surrounding h-BN layers and only consider the dielectric screening due to the h-BN layers, i.e., $D_{lv,l'v'} = \delta_{l0}\delta_{l'0}D_{lv,l'v'}$. The second approach considers the remote phonon scattering but ignores the remote phonon coupling, and thus is called "ph isolated" here. The D is assumed to be: $D_{lv,l'v'} = \delta_{ll'}D_{lv,l'v'}$. The third approach is the most accurate and consider the full D matrix and is called "all coupled".

The InSe Fröhlich mobility using different calculation approaches in InSe/BN vdW heterostructure is shown in Fig. 2a. The Fröhlich mobility of suspended InSe monolayer is 125 cm^{2}V^{-1}s^{-1}, slightly higher than its total mobility 117 cm^{2}V^{-1}s^{-1} from first-principles calculations, indicating the carrier transport in InSe is limited by Fröhlich scattering. As shown in Fig. 2d, the Fröhlich

scattering from our model (blue line) is consistent with the Fröhlich scattering calculated from more accurate model via EPW (grey scatter). When stacked with BN multilayers, the Fröhlich mobility increases with number of BN layers but converges at 7 layers of BN (~2.3 nm). When wrapped by BN from both sides, the InSe Fröhlich mobility can be further enhanced up to 304 cm^{2}V^{-1}s^{-1} due to stronger coupling between the InSe and BN layers. The InSe mobility enhancement has two origins: First, the electrons in BN layers provide dielectric screening and reduce the Fröhlich potential induced by POPs in InSe. It can be seen from "all isolated" approach (blue line) in Fig. 2a, which excludes the remote phonon from BN layers but considers the dielectric screening via $W_{l'l}$ in g^F (Eq. 9). Fig. 2d shows the "all isolated" scattering rate of InSe with different BN layers. Indeed, the dielectric screening increases with the number of BN layers, and consequently decreases the Fröhlich scattering.

Another mobility increase originates from the POP coupling between BN layers and InSe layers. As shown in Fig. 2a, the introduction of remote phonon in BN will slightly decrease the Fröhlich mobility compared to "all isolated" approach, without turning on interlayer phonon coupling (yellow line). However, when phonon coupling is considered in "coupled" approach, the InSe Fröhlich mobility can be further increased by 15 cm^{2}V^{-1}s^{-1} in one-side model and 40 cm^{2}V^{-1}s^{-1} in double-side model (gree line in Fig. 2a). The mobility improvement can be understood because the Fröhlich potential is screened due to the lattice vibration, in addition to the dielectric screening from electrons. Here we take the InSe/1L-BN as a simplest example. As shown in diagram in Fig. 1d (left column), the isolated BN has a larger POP frequency (>0.16 eV) while the POP of InSe monolayer locates at a lower energy (~0.02 eV). Once a weak POP coupling is included into model, the two previous POP states will give rise to two coupled vibrations and two new eigenvalues (right column in Fig. 1d). The new coupled LO$_1$ has larger frequency due to the stronger electrostatic field contributed by both POPs in BN and InSe. The coupled LO$_2$ will have opposite POP vibration and thus a weaker Fröhlich potential compared to original InSe POP. This can be easily understood from a two-level model dynamical matrix:

$$D = \begin{pmatrix} \omega_1^2 & \eta \\ \eta & \omega_2^2 \end{pmatrix} \tag{10}$$

where ω_1 is the lower InSe POP frequency and the ω_2 is the larger BN POP frequency, and η is the POP coupling. When the $\eta=0$, the eigenvectors of D are $u_1=(1, 0)$ and $u_2=(0, 1)$, representing the pure InSe POP and BN POP vibration respectively. When the POP coupling $\eta>0$ due to the Coulomb interaction, the diagonalization of Eq. 10 gives two hybrid eigen-vibrations:

$$u_1 = (1, \quad -\sin\theta)$$
$$u_2 = (\sin\theta, \quad 1) \tag{11}$$
$$\sin 2\theta = \frac{2\eta}{\sqrt{\omega_2^2 - \omega_1^2 + 4\eta^2}}$$

The u_1 indicates the pure InSe POP is combined with a small component of opposite BN POP while the u_2 means the BN POP is accompanied by an aligned small InSe POP vibration. The u_1 generally has a weaker Fröhlich potential than pure InSe POP vibration, due to the lattice screening from -sinθ component of BN vibration.

The above inferences derived from the simple two-level model can be verified via our more

accurate Fröhlich model. Indeed, we found the hybrid POP frequency changes as indicated by Fig. 1d in vdW heterostructure. In Fig. 2g, the uncoupled and the coupled POP frequency are plotted by dashed lines and solid lines, respectively. Note here we used a similar InSe/HfO$_2$ system, which shows the frequency difference more clearly. The lower hybrid POP has lower frequency than the original uncoupled ones while the higher hybrid POP has higher frequency. The hybrid POP also weakens the Fröhlich potential for InSe POP and thus leads to lower scattering rates as shown in Fig. 2b in InSe/1L-BN system. The first scattering rate peak around 0.02 eV corresponds to the InSe POP and the second peak (~0.18 eV) indicates the Fröhlich scattering due to POP in BN. In comparison to "ph isolated" without POP coupling, the "coupled" approach (red line) gives slightly lower scattering rate due to the lattice screening from the BN layer. The lattice screening can be further increased by more BN layers. As shown in Fig. 2e, the scattering rate difference with (red line) and without (green line) POP coupling is larger than Fig. 2b, due to 5 layers of BN is included in InSe/BN vdW heterostructure. The 5 layers of BN also display more complicated hybrid POPs with different frequency (see right part in Fig. 2h), which leads to multiple POP peaks around 0.18 eV in Fig. 2e.
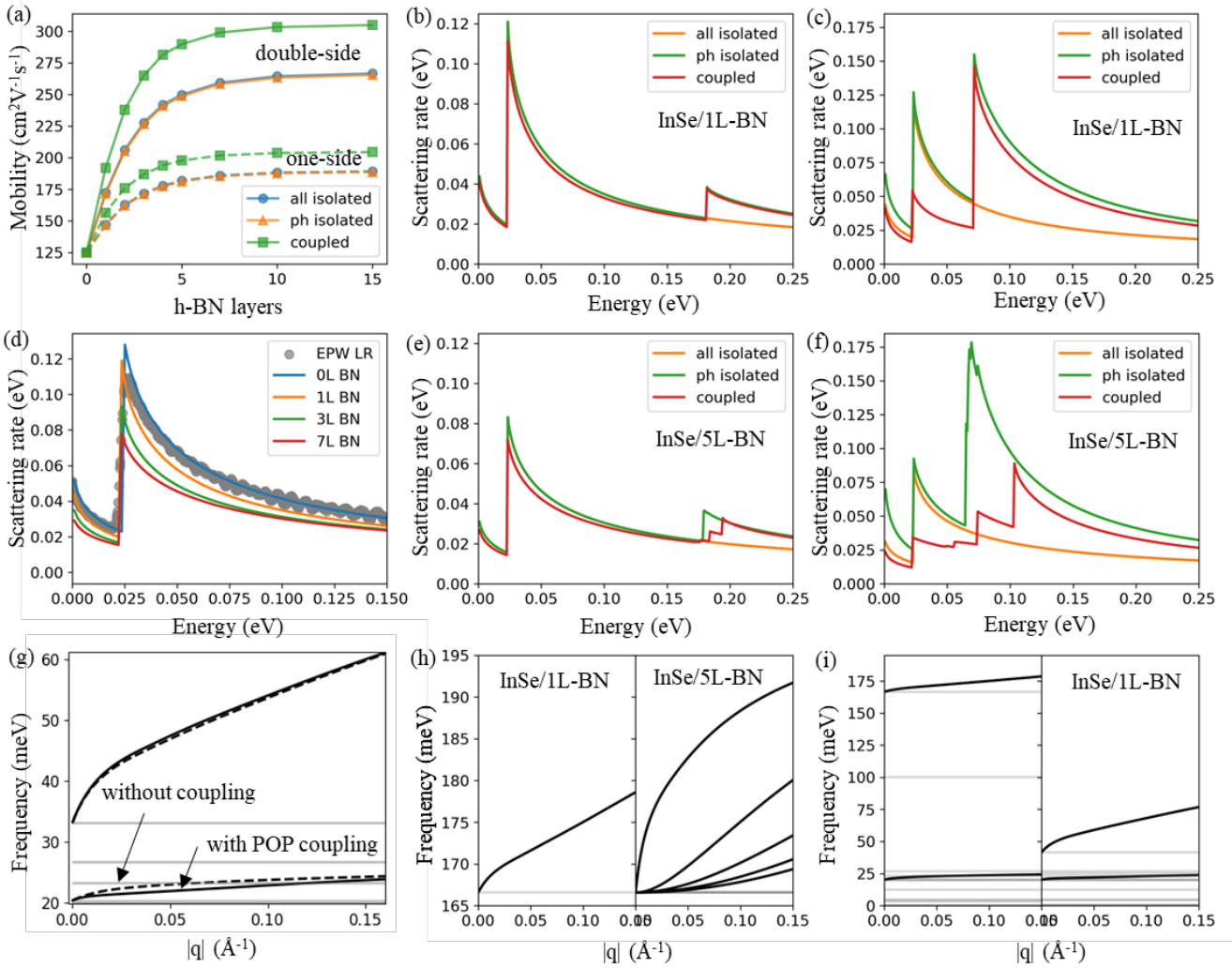
Figure 2. (a) Mobility of InSe monolayer in InSe/BN vdW heterostructure using different calculation approaches. The "double-side" indicates the InSe is embedded in BN layers and "one-side" means the

h-BN is stacked on one side of InSe. (b), (e) The scattering rates of InSe in vdW heterostructure consisting of InSe/1L-BN and InSe/5L-BN. (c), (f) Similar to (b), (e) but the dynamical matrix of BN is modified to 1/16. (d) The scattering rate of InSe in InSe/nL-BN system, using the "all isolated" method. The grey scatters indicate the Fröhlich scattering from first principles calculations. (g) The frequency of InSe/HfO$_2$ system using "all isolated" (dashed line) and "all coupled" (solid line) approaches. (h) The comparison of frequency in "all coupled" InSe/1L-BN and InSe/5L-BN systems. (i) Comparison of InSe/1L-BN frequency between original BN dynamical matrix and modified BN dynamical matrix (1/16).

The overall screening from surrounding layers, dielectric screening from electrons and lattice screening from remote phonons, on Fröhlich potential lead to InSe mobility improvement from 125 to 304 cm^{2}V^{-1}s^{-1}, with 15 layers of BN on both sides of InSe respectively. This leads to another question: How will other 2D materials enhance the InSe mobility in vdW heterostructure? Before doing real calculations with other 2D materials, here we modify the frequency and Born effective charges of BN and use these "artificial" BN layers as surrounding layers in InSe/BN vdW heterostructure to see how these two factors affect the InSe Fröhlich mobility.

The influence of POP frequency of surrounding layers on InSe Fröhlich mobility can be seen in Fig. 2cf. The frequency of BN can be modified by reducing the analytic part of dynamical matrix D^a. Modifying the D^a to 1/16 leads to POP BN frequency at $\mathbf{q}$=0 (ω_0) decreasing to 1/4, i.e., the BN ω_0 reduces to 0.04 eV as shown in right part of Fig. 2i. Compared to original BN with ω_0=0.16 eV in Fig. 2be, the lower ω_0=0.04 eV of the surrounding layers in Fig. 2cf has mainly two consequences on InSe Fröhlich scattering rate. (1) The lower ω_0 leads to stronger remote phonon scattering due to larger phonon occupation. As shown in Fig. 2c, the scattering rate around 0.04 eV corresponding to remote POP scattering is more significant than the remote POP scattering peak around 0.16 eV in Fig. 2b, and is supposed to decrease the InSe mobility. (2) The POP coupling is strengthened as well and the lattice screening from the surrounding layers is more obvious. Note that the scattering rate peak around 0.02 eV in Fig. 2c is much lower due to the strong lattice screening than Fig. 2b. This can be understood from Eq. 11. The lattice screening in coupled POP (characterized by -sinθ) increases as the (ω^2_2-ω^2_1) decreases, resulting in lower scattering rates and a larger InSe mobility. The overall InSe Fröhlich mobility is determined by the trade-off of the decrease of the InSe scattering and increase of the remote POP scattering. The Fig. 3a shows the Fröhlich mobility of InSe wrapped by double-side 7L BN with different POP ω_0. Indeed, the "coupled" InSe Fröhlich mobility shows a non-monotonical change with respect to POP ω_0. A lower POP ω_0 will introduce strong remote phonon scattering, leading to degradation of InSe Fröhlich mobility, while a larger POP ω_0 will result in weak POP coupling, weak lattice screening and thus lower InSe mobility. The optimal POP ω_0 is around 0.06 eV and gives a largest InSe mobility around 360 cm^{2}V^{-1}s^{-1}. Note that the "ph isolated" method, which ignores the POP coupling, will severely underestimate the InSe Fröhlich mobility in vdW heterostructure, especially with small POP ω_0 (e.g. < 50 meV).

Another important factor on lattice screening of Fröhlich scattering is the Born effective charges BCs of surrounding layers. From Eqs. 7 and 8, the off-diagonal term in dynamical matrix is proportional to BCs. Therefore, larger BCs will lead to larger η in Eqs. 10 and 11 and a larger lattice screening component (i.e. -sinθ) in u_1. In Fig. 3b, we modify the BCs of BN (from 0.27 to 10.8; the

BC of BN is 2.7) and calculate the InSe Fröhlich mobility in double-side InSe/7L-BN system. Note that we used a more delicate quantity $\Delta\omega$ which contains all components of off-diagonal term in dynamical matrix in addition to BCs. The $\Delta\omega$ is defined as:

$$\Delta\omega = \frac{ez_{\mathrm{POP}}}{\sqrt{\alpha^{\parallel}A}} \tag{12}$$

where e is the electron charge, z_{POP} is the effective Born effective charges corresponding to POP defined in Eq. 8, $\alpha^{\parallel}$ is in-plane polarizability of the 2D materials and A is the area of unit cell. The $\Delta\omega$ is approximately the frequency difference of the POP frequency at $|\mathbf{q}|\gg1$ and $|\mathbf{q}|=0$ (see Appendix B). As shown in Fig. 3b, the InSe mobility continuously increases with the $\Delta\omega$, indicating a larger $\Delta\omega$ is more desirable for surrounding layers in vdW. It is counterintuitive since a larger $\Delta\omega$ usually means larger BCs, lower dielectric screening and thus stronger remote phonon scattering. However, the large $\Delta\omega$ of surrounding layers benefits the InSe Fröhlich mobility in two fashions: (1) A larger $\Delta\omega$ leads to larger POP coupling, enhances the lattice screening, and thus increases the InSe Fröhlich mobility. (2) The $\Delta\omega$ also generates a large POP frequency at $|\mathbf{q}|>0$ given the same ω_0, leading to lower phonon occupations and thus lower remote phonon scattering.
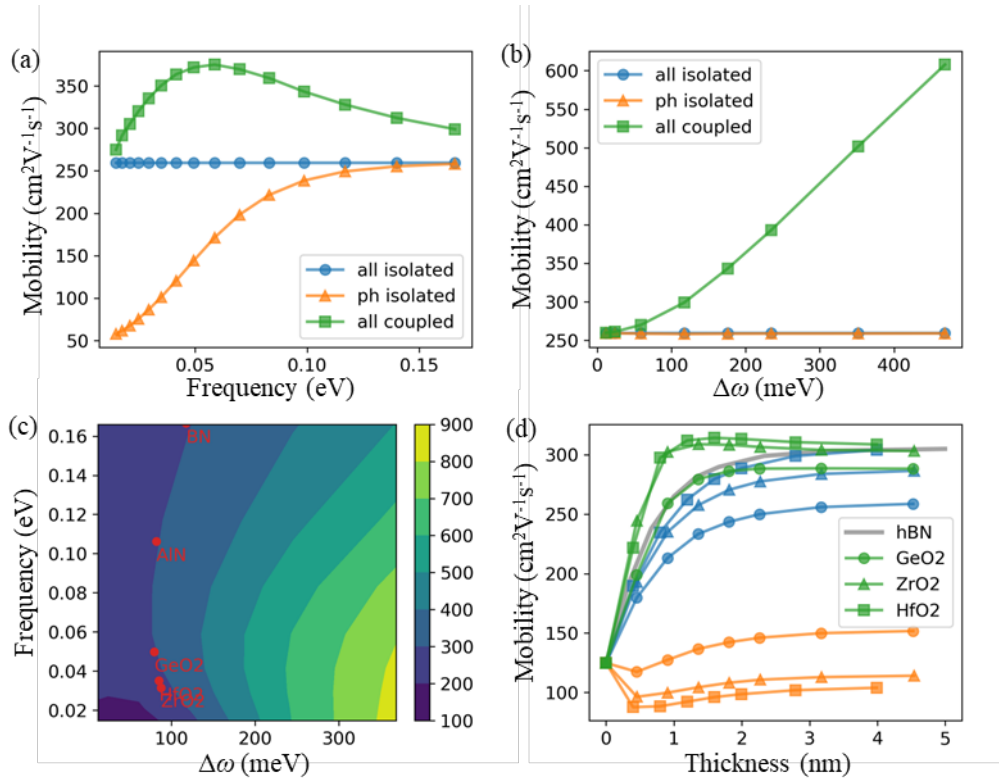
Figure 3. (a) The InSe Fröhlich mobility calculated via different approaches, in double-side InSe/7L-BN vdW heterostructure. The BN monolayer frequency is modified and the POP frequency at $\mathbf{q}=0$ (ω_0) is shown in x axis. (b) Similar to (a) but the Born effective charges of BN are modified. The x axis shows frequency increase $\Delta\omega$ (see Eq. 12 for definition). (c) The InSe Fröhlich mobility in double-side InSe/7L-BN vdW heterostructure, with different POP frequency at $\mathbf{q}=0$ (ω_0) and POP frequency increase ($\Delta\omega$). (d) The Fröhlich mobility of InSe wrapped by 7 layers of GeO$_2$, ZrO$_2$ and HfO$_2$ from

different calculation approaches. The blue, yellow and green lines indicate "all isolated", "ph isolated" and "coupled" approaches respectively.

In Fig. 3c, we show the overall influence of POP frequency at $\mathbf{q}$=0 (ω_0) and POP frequency increase ($\Delta\omega$) on Fröhlich mobility of InSe in double-side 7L-BN vdW heterostructure. The lowest and highest InSe mobility occur at the left-lower corner and right-lower corner, respectively. At the left-lower corner, the low ω_0 in conjunction with the low $\Delta\omega$ contribute to the low POP frequency in the surrounding layers, leading to higher phonon occupations, stronger remote phonon scattering and thus lower InSe Fröhlich mobility. Moreover, the low $\Delta\omega$ indicates smaller POP coupling (i.e. smaller η in Eq. 10), which reduces the lattice screening and InSe mobility. The highest InSe mobility appears with the combination of large $\Delta\omega$ and low ω_0, both of which lead to stronger lattice screening (i.e. -$\sin\theta$ in Eq. 11) between the surrounding layers and the InSe. The larger $\Delta\omega$ implies larger POP coupling (η) and lower ω_0 means smaller POP frequency difference between surrounding layers and InSe ($\omega_2^2 - \omega_1^2$), both resulting in larger $\sin 2\theta$ (Eq. 11) and stronger lattice screening. At fixing $\Delta\omega$, the InSe mobility shows a non-monotonical trend with ω_0, which is consistent with Fig. 3a. In contrast, with a given a ω_0, the InSe mobility increases monotonically with $\Delta\omega$, in agreement with Fig. 3b. In general, the InSe Fröhlich mobility has a stronger dependence on $\Delta\omega$, hopefully leading to an extremely high InSe mobility > 700 cm^{2}V^{-1}s^{-1} once $\Delta\omega$ > 300 meV.

In the following, we explore optimal dielectrics for high InSe mobility using the knowledge from above analysis. Using Computational 2D Materials Database (C2DB) [26,27] containing more than 4000 2D materials, we extract and calculate the desirable quantities for optimal dielectrics, screen the C2DB database through 3 steps: (1) First, we identify insulators with electronic band gaps over 3 eV. Note that here we used the HSE bandgap which is more accurate. (2) Then we exclude those lack of "dynamical stability" and "stiffness stability" as labelled by the database. (3) For the remaining materials, we calculate the $\Delta\omega$ corresponding to their lowest POP mode and use $\Delta\omega$ as the only descriptor in search for the optimal dielectrics. This is because from Fig. 3c we found the $\Delta\omega$ is the more important factor than ω_0 for InSe Fröhlich mobility. The top 5 2D materials with largest $\Delta\omega$ are plotted in Fig. 3c, including BN, ZrO_2, HfO_2, AlN and GeO_2, in the descending order of $\Delta\omega$. As we can see from Fig. 3c, these new 2D dielectric materials are close to the iso-mobility contour with 300 cm^{2}V^{-1}s^{-1}, similar to BN. Indeed, in Fig. 3d, the Fröhlich mobility of InSe in doube-side vdW heterostructure consisting of different dielectric materials has similar upper limit (~ 300 cm^{2}V^{-1}s^{-1}) for BN, GeO_2, ZrO_2 and HfO_2. Although the InSe mobility wrapped by ZrO_2, HfO_2 and GeO_2 is not significantly better than that with BN, the wider bandgap and larger dielectric constants of ZrO_2, HfO_2 and GeO_2 are likely to lead to smaller leakage currents [28] than BN, making them more promising as dielectric materials in 2D nanoelectronics. It is also worth noting that in Fig. 3d the difference between "ph isolated" (yellow line) and "coupled" (green line) mobility can be up to 3 times, indicating the importance of POP coupling in InSe Fröhlich mobility calculations.

Conclusion:

In this work, we developed an efficient model to evaluate the Fröhlich mobility of 2D materials in vdW heterostructure. Using InSe/BN vdW heterostructure as an example, we showed that the Fröhlich mobility of InSe surrounded by BN layers can be up to 300 $cm^2V^{-1}s^{-1}$, nearly 2.5 times of Fröhlich mobility of suspended InSe monolayer. The change of mobility has mainly 3 contributions: the dielectric screening from surrounding layers, the remote phonon scattering of remote polar-optical phonons (POPs), and the POP coupling via Coulomb interaction leading to change of Fröhlich scattering strength. We found the POP coupling is of great importance for correct Fröhlich scattering in vdW heterostructure, which generates additional lattice screening for Fröhlich potential and could provide 3 times of mobility enhancement compared to that without POP coupling. Exemplified by InSe/BN system, we uncovered the fundamental physical properties that lead to optimal Fröhlich mobility in InSe: moderate POP frequency at $\mathbf{q}$=0 (ω_0) and larger POP frequency increase ($\Delta\omega$). Using these descriptors, we filtered out more potential 2D dielectric insulators for vdW heterostructures, e.g., AlN, GeO_2, ZrO_2 and HfO_2. The discovered materials as well as the mechanistic insights bring us a step closer to the next-generation electronics/optoelectronics.

[1] A. K. Geim and I. V. Grigorieva, Nature **499**, 419 (2013).

[2] Y. Liu, N. O. Weiss, X. Duan, H.-C. Cheng, Y. Huang, and X. Duan, Nature Reviews Materials **1**, 1 (2016).

[3] K. S. Novoselov, A. Mishchenko, A. Carvalho, and A. H. C. Neto, Science **353** (2016).

[4] L. Cheng, C. Zhang, and Y. Liu, Phys. Rev. Lett. **125**, 177701 (2020).

[5] C. Zhang and Y. Liu, Phys. Rev. B **106** (2022).

[6] T. Sohier, D. Campi, N. Marzari, and M. Gibertini, Phys. Rev. Materials **2**, 114010 (2018).

[7] S. Poncé, M. Royo, M. Gibertini, N. Marzari, and M. Stengel, (arXiv, 2022).

[8] L. Cheng and Y. Liu, J. Am. Chem. Soc. **140**, 17895 (2018).

[9] S. Gopalan, G. Gaddemane, M. L. Van de Put, and M. V. Fischetti, Materials **12**, 4210 (2019).

[10] L. Wendler, Physica status solidi (b) **129**, 513 (1985).

[11] N. Mori and T. Ando, Phys. Rev. B **40**, 6175 (1989).

[12] B. Lee, K. Kim, M. Stroscio, and M. Dutta, Phys. Rev. B **58**, 4860 (1998).

[13] M. V. Fischetti, D. A. Neumayer, and E. A. Cartier, Journal of Applied Physics **90**, 4587 (2001).

[14] X. J. Zhou, Z. Gu, S. L. Ban, and Z. P. Wang, Journal of Applied Physics **120**, 125706 (2016).

[15] B. Laikhtman and P. M. Solomon, Journal of Applied Physics **103**, 014501 (2008).

[16] L. Zhang, J.-j. Shi, and T. L. Tansley, Phys. Rev. B **71**, 245324 (2005).

[17] S. Fratini and F. Guinea, Phys. Rev. B **77**, 195415 (2008).

[18] A. Konar, T. Fang, and D. Jena, Phys. Rev. B **82**, 115452 (2010).

[19] Z.-Y. Ong and M. V. Fischetti, Phys. Rev. B **86**, 165422 (2012).

[20] Z.-Y. Ong and M. V. Fischetti, Phys. Rev. B **88**, 045405 (2013).

[21] L. Zeng, Z. Xin, S. Chen, G. Du, J. Kang, and X. Liu, Appl. Phys. Lett. **103**, 113505 (2013).

[22] N. Ma and D. Jena, Phys. Rev. X **4**, 011043 (2014).

[23] S. Baroni, S. de Gironcoli, A. Dal Corso, and P. Giannozzi, Rev. Mod. Phys. **73**, 515 (2001).

[24] K. Andersen, S. Latini, and K. S. Thygesen, Nano Lett. **15**, 4616 (2015).

[25] M. N. Gjerding, L. S. R. Cavalcante, A. Chaves, and K. S. Thygesen, J. Phys. Chem. C **124**, 11609 (2020).

[26] S. Haastrup *et al.*, 2D Mater. **5**, 042002 (2018).

[27] M. N. Gjerding *et al.*, 2D Mater. **8**, 044002 (2021).

[28] Y. Y. Illarionov *et al.*, Nat Commun **11**, 3385 (2020).

Realistic Fröhlich Scattering and Mobility of 2D Semiconductors

in van der Waals Heterostructure

Chenmu Zhang, Yuanyue Liu[*]

Texas Materials Institute and Department of Mechanical Engineering,

The University of Texas at Austin, Austin, Texas 78712, USA

Yuanyue.liu@austin.utexas.edu

Appendix A: Dynamical matrix and Fröhlich coupling in vdW heterostructure

The Hamiltonian of lattice vibration in a vdW heterostructure can be written as:

$$H_{\text{tot}} = H_{\text{tot}}^a + V_{\text{tot}}^{na} = T_{\text{tot}} + V_{\text{tot}}^a + V_{\text{tot}}^{na} \tag{1}$$

where T is the kinetic energy term, V^a is the analytic potential term due to the short-range interaction and V^{na} is the nonanalytic potential term leading from long-range Coulomb interaction [1]. Here we assume the interlayer distance is large and thus the interlayer coupling in Eq. 1 only comes from the V^{na} term. Therefore, the H^a in Eq. 1 can be decomposed to individual layers:

$$H_{\text{tot}}^a = \sum_l H_l^a \tag{2}$$

and H^a is:

$$H_l^a = \sum_{p\alpha i} -\frac{1}{2M_\alpha}\frac{\partial^2}{\partial h_{pl\alpha i}^2} + \frac{1}{2}\sum_{p\alpha i}\sum_{p'\alpha'i'} D_{l\alpha i,l\alpha'i'}^a(\mathbf{R}_p,\mathbf{R}_{p'})h_{pl\alpha i}h_{p'l\alpha'i'} \tag{3}$$

where p is the index of unit cell in the whole supercell, α is the atom index in the unit cell, i is cartesian index in x, y, z; h is the atomic displacement from their equilibrium positions, $\mathbf{R}$ is the position of the unit cell, M is the atomic mass and D^a is the force constants due to the short-range interaction. A standard solution to Eq. 3 is to transform the coordinates $h_{pl\alpha i}$ into a set of complex normal coordinates $u_{\mathbf{q}l\nu}$:

$$
\begin{aligned}
u_{\mathbf{q}l\nu} &= \frac{1}{\sqrt{N_l}}\sum_{p\alpha i}\sqrt{M_{l\alpha}}h_{pl\alpha i}e^{-i\mathbf{q}\cdot\mathbf{R}_p}e_{-\mathbf{q}l\nu;\alpha i} \\
h_{pl\alpha i} &= \frac{1}{\sqrt{N_l}}\sum_{\mathbf{q}\in Q_l,\nu}\frac{1}{\sqrt{M_{l\alpha}}}u_{\mathbf{q}l\nu}e^{i\mathbf{q}\cdot\mathbf{R}_p}e_{\mathbf{q}l\nu;\alpha i}
\end{aligned}
\tag{4}
$$

where $e_{\mathbf{q}l\nu}$ is the eigenvectors of analytic dynamical matrix $D^a(\mathbf{q})$:

$$\sum_{\alpha'i'} D_{l\alpha i,l\alpha'i'}^a(\mathbf{q})e_{\mathbf{q}l\nu;\alpha'i'} = \omega_{\mathbf{q}\nu}^2 e_{\mathbf{q}l\nu;\alpha i} \tag{5}$$

and $D^a(\mathbf{q})$ is the Fourier transform of force constants:

$$D_{l\alpha i,l\alpha'i'}^a(\mathbf{q}) = \sum_p \frac{1}{\sqrt{M_\alpha M_{\alpha'}}} D_{l\alpha i,l\alpha'i'}^a(0,\mathbf{R}_p)e^{i\mathbf{q}\cdot\mathbf{R}_p} \tag{6}$$

Inserting h from Eq. 4 into Eq. 3 and combining Eqs. 5 and 6, the H^a for the whole vdW heterostructure can be written as:

$$H_{\text{tot}}^a = \sum_l \sum_{\mathbf{q} \in Q_l, v} \frac{1}{2} \left(\frac{\partial}{\partial u_{\mathbf{q}lv}} \frac{\partial}{\partial u_{\mathbf{q}lv}^*} + \omega_{\mathbf{q}lv}^2 u_{\mathbf{q}lv} u_{\mathbf{q}lv}^* \right) \tag{7}$$

Before explicitly expressing the interlayer coupling term V^{na}, here we give necessary descriptions on boundary conditions used in the vdW heterostructure system. The BvK boundary conditions assume each layer contains $N_l = N_{l1} \times N_{l2}$ unit cells, since each layer is periodic in xy plane. The total area of the supercell is denoted as A and the area of the unit cell is A_l, indicating $A_{\text{tot}} = N_l A_l = N_{l'} A_{l'}$. Here we assume the primitive lattice vectors of each layer have the same direction for simplicity (This is not necessary since we are only interested in zone-center properties). We have such relations of primitive lattice $\mathbf{a}_{li}$ and reciprocal lattice $\mathbf{b}_{lj}$:

$$N_{li} \mathbf{a}_{li} = N_{l'i} \mathbf{a}_{l'i}$$
$$\frac{\mathbf{b}_{li}}{N_{li}} = \frac{\mathbf{b}_{l'i}}{N_{l'i}} \tag{8}$$

The Bloch wave vectors $\mathbf{q}_l$ for each layer fall on a uniform grid:

$$\mathbf{q}_l = \sum_j m_j \frac{\mathbf{b}_{lj}}{N_{lj}}, \, m_j = 0, \cdots, N_{lj} - 1 \tag{9}$$

From Eq. 8, the $\mathbf{q}_l$ have common values around the zone-center for all l layers.

The Coulomb screened potential generated by dipole induced by atomic displacement $h_{pl\alpha i}$ from layer l is [2]:

$$V_l^c(\mathbf{r}; h_{pl\alpha i}) = \frac{-ie}{A_{\text{tot}}} \sum_{\mathbf{q}} W_l(\mathbf{q}, z)(\mathbf{q} \cdot \mathbf{Z}_{l\alpha}^*)_i h_{pl\alpha i} e^{i\mathbf{q} \cdot (\mathbf{r} - \mathbf{R}_p - \boldsymbol{\tau}_{l\alpha})} \tag{10}$$

The $W_l(\mathbf{q}, z)$ is the screened potential with in-plane reciprocal lattice vector $\mathbf{q}$ and out-of-plane real space coordinate z, which can be calculated in QEH model [3,4] (see Appendix B for details). Note here we drop the subscript l of $\mathbf{q}$ since we are only interested in zone-center properties (W is considered as a long-range interaction and vanishes when $|\mathbf{q}|$ is large) and the $\mathbf{q}_l$ have same values around zone-center. The interaction energy between dipole induced by atomic displacement $h_{pl\alpha i}$ and dipole from $h_{p'l'\alpha'i'}$ is:

$$V_{ll'}^c(h_{p'l'\alpha'i'}; h_{pl\alpha i}) = \frac{e^2}{A_{\text{tot}}} \sum_{\mathbf{q}} \frac{W_{ll'}(\mathbf{q}) + W_{l'l}(\mathbf{q})}{2} (\mathbf{q} \cdot \mathbf{Z}_{l'\alpha'}^*)_{i'} (\mathbf{q} \cdot \mathbf{Z}_{l\alpha}^*)_i h_{p'l'\alpha'i'} h_{pl\alpha i} e^{i\mathbf{q} \cdot (\mathbf{R}_{p'} - \mathbf{R}_p)} e^{i\mathbf{q} \cdot (\boldsymbol{\tau}_{l'\alpha'} - \boldsymbol{\tau}_{l\alpha})} \tag{11}$$

where $W_{ll'}(\mathbf{q})$ is the screened potential matrix which can be obtained from QEH model. The V^{na} in Eq. 1 thus can be written as:

$$V_{\text{tot}}^{na} = \frac{1}{2} \sum_{l'p'\alpha'i'} \sum_{lp\alpha i} V_{ll'}^c(h_{p'l'\alpha'i'}; h_{pl\alpha i}) \tag{12}$$

Inserting h (Eq. 4) into Eq. 12 and applying orthogonal normalization relations:

$$\sum_{\mathbf{q} \in Q_l} e^{i\mathbf{q} \cdot \mathbf{R}_p} = N_l \delta_{p0}$$

$$\sum_{p \in P_l} e^{i\mathbf{q} \cdot \mathbf{R}_p} = N_l \delta_{\mathbf{q}0}$$

(13)

We can write the V^{na} in normal coordinates $u_{\mathbf{q}lv}$:

$$V_{\text{tot}}^{na} = \frac{e^2}{2} \sum_{\mathbf{q}} \sum_{ll',vv'} u_{\mathbf{q}lv} u_{\mathbf{q}l'v'}^* z_{lv} z_{l'v'}^* \frac{|\mathbf{q}|^2 \bar{W}_{ll'}(\mathbf{q})}{\sqrt{A_l A_{l'}}}$$

(14)

where $\bar{W}_{ll'}(\mathbf{q}) = [W_{ll'}(\mathbf{q}) + W_{l'l}(\mathbf{q})]/2$ and z_{lv} is:

$$z_{lv} = \sum_{\alpha i} \frac{(\hat{\mathbf{q}} \cdot \mathbf{Z}_{l\alpha}^*)_i e_{\mathbf{q}lv;\alpha i}}{\sqrt{M_{l\alpha}}}$$

(15)

Writing the Eq. 14 with a dynamical matrix form:

$$V_{\text{tot}}^{na} = \frac{1}{2} \sum_{\mathbf{q}} \sum_{ll'vv'} D_{lv,l'v'}^{na}(\mathbf{q}) u_{\mathbf{q}lv} u_{\mathbf{q}l'v'}^*$$

(16)

Therefore, the dynamical matrix can be deduced by comparing Eqs. 14 and 16:

$$D_{lv,l'v'}^{na}(\mathbf{q}) = e^2 z_{lv} z_{l'v'}^* \frac{|\mathbf{q}| \bar{W}_{ll'}(\mathbf{q})}{\sqrt{A_l A_{l'}}}$$

(17)

With H^a from Eq. 7 and V^{na} from Eq. 16, now we have all the ingredients in Hamiltonian of lattice vibration H_{tot}. Around the zone-center, the H_{tot} can be written with normal coordinates $u_{\mathbf{q}lv}$:

$$H_{\text{tot}} = \frac{1}{2} \sum_{\mathbf{q}} \sum_{ll'vv'} \left[\delta_{ll'} \delta_{vv'} \frac{\partial}{\partial u_{\mathbf{q}lv}} \frac{\partial}{\partial u_{\mathbf{q}lv}^*} + \left(\delta_{ll'} \delta_{vv'} \omega_{\mathbf{q}lv}^2 + D_{lv,l'v'}^{na}(\mathbf{q}) \right) u_{\mathbf{q}lv} u_{\mathbf{q}lv}^* \right]$$

(18)

which gives a new dynamical matrix of vdW lattice vibration including long-range interlayer phonon coupling:

$$D_{lv,l'v'}(\mathbf{q}) = \delta_{ll'} \delta_{vv'} \omega_{\mathbf{q}lv}^2 + e^2 z_{lv} z_{l'v'}^* \frac{|\mathbf{q}|^2 \bar{W}_{ll'}(\mathbf{q})}{\sqrt{A_l A_{l'}}}$$

(19)

The $\omega_{\mathbf{q}lv}$ is calculated from diagonalizing the analytic dynamic matrix D^a, which should be smooth around the zone-center. By replacing $\omega_{\mathbf{q}lv}$ as $\omega_{\mathbf{0}lv}$ which is calculated from $D^a(\mathbf{q}=0)$, we obtain the Eq. 7 in the main text.

Next we diagonalize the D in Eq. 19 and then we are able to obtain the hybrid vibration of vdW heterostructure. Similar to Eq. 5, the $\tilde{e}_{\mathbf{q}\mu;lv}$, $\tilde{\omega}_{\mathbf{q}\mu}^2$ are eigenvectors and eigenvalues of dynamical matrix D, respectively:

$$\sum_{l'v'} D_{lv,l'v'}(\mathbf{q}) \tilde{e}_{\mathbf{q}\mu;l'v'} = \tilde{\omega}_{\mathbf{q}\mu}^2 \tilde{e}_{\mathbf{q}\mu;lv}$$

(20)

With $\tilde{e}_{\mathbf{q}\mu;lv}$, we are able to transform the normal coordinates $u_{\mathbf{q}lv}$ into a set of new complex normal coordinates $U_{\mathbf{q}\mu}$:

$$U_{\mathbf{q}\mu} = \sum_{lv} \tilde{e}^*_{\mathbf{q}\mu;lv} u_{\mathbf{q}lv} \tag{21}$$

The Hamiltonian of lattice vibration H_{tot} is diagonal with complex normal coordinates $U_{\mathbf{q}\mu}$:

$$H_{\text{tot}} = \sum_{\mathbf{q}} \sum_{\mu} \frac{1}{2} \left(\frac{\partial}{\partial U_{\mathbf{q}\mu}} \frac{\partial}{\partial U^*_{\mathbf{q}\mu}} + \tilde{\omega}^2_{\mathbf{q}\mu} U_{\mathbf{q}\mu} U^*_{\mathbf{q}\mu} \right) \tag{22}$$

With the frequency of hybrid phonon $\tilde{\omega}_{\mathbf{q}\mu}$, we are able to calculate the Fröhlich electron-phonon coupling $\bar{g}^{\text{F}}$. Following the definition in [5], the $\bar{g}^{\text{F}}$ in BvK boundary conditions is defined as:

$$\bar{g}^{\text{F}}_{l\mu}(\mathbf{k},\mathbf{q}) = \langle \psi_{l\mathbf{k}+\mathbf{q}} | \frac{-e}{\sqrt{2\tilde{\omega}_{\mathbf{q}\mu}}} \frac{\partial V^c_l(\mathbf{r})}{\partial U_{\mathbf{q}\mu}} | \psi_{l\mathbf{k}} \rangle \tag{23}$$

where $\psi_{l\mathbf{k}}$ is the wavefunction with wavevector $\mathbf{k}$ in layer l and $V^c_l(\mathbf{r})$ is the total Fröhlich perturbation potential acting on layer l:

$$V^c_l(\mathbf{r}) = \sum_{p\alpha i} V^c_l(\mathbf{r}; h_{pl\alpha i}) \tag{24}$$

where $V^c_l(\mathbf{r}; h_{pl\alpha i})$ is Fröhlich perturbation potential due to atomic displacement $h_{pl\alpha i}$ defined in Eq. 10. Inserting $h_{pl\alpha i}$ (Eq. 4) into Eq. 24, we have:

$$V^{\text{F}}_l(\mathbf{r}) = \frac{-ie}{A_l} \sum_{\mathbf{q}v} \frac{1}{\sqrt{N_l}} W_l(\mathbf{q},z) z_{lv} u_{\mathbf{q}lv} e^{i\mathbf{q}\cdot\mathbf{r}} \tag{25}$$

It is obvious that from Eq. 25, we have:

$$\frac{\partial V^{\text{F}}_l(\mathbf{r})}{\partial u_{\mathbf{q}lv}} = \frac{-ie}{A_l} \frac{1}{\sqrt{N_l}} |\mathbf{q}| W_l(\mathbf{q},z) z_{lv} \tag{26}$$

With Eq. 26 and Eq. 21, finally we can calculate the $\bar{g}^{\text{F}}$ (in Eq. 23) by:

$$\begin{aligned}
\bar{g}^{\text{F}}_{l\mu}(\mathbf{k},\mathbf{q}) &= \langle \psi_{l\mathbf{k}+\mathbf{q}} | \frac{-e}{\sqrt{2\tilde{\omega}_{\mathbf{q}\mu}}} \frac{\partial V^c_l(\mathbf{r})}{\partial U_{\mathbf{q}\mu}} | \psi_{l\mathbf{k}} \rangle \\
&= \langle \psi_{l\mathbf{k}+\mathbf{q}} | \frac{-e}{\sqrt{2\tilde{\omega}_{\mathbf{q}\mu}}} \sum_{l'v} \frac{\partial V^c_{l'}(\mathbf{r})}{\partial u_{\mathbf{q}l'v}} \frac{\partial u_{\mathbf{q}l'v}}{\partial U_{\mathbf{q}\mu}} | \psi_{l\mathbf{k}} \rangle \\
&= \sum_{l'v} \frac{\tilde{e}_{\mathbf{q}\mu;l'v}}{\sqrt{2\tilde{\omega}_{\mathbf{q}\mu}}} \frac{ie^2}{A_{l'}} \frac{1}{\sqrt{N_{l'}}} |\mathbf{q}| z_{l'v} \langle \psi_{l\mathbf{k}+\mathbf{q}} | W_{l'}(\mathbf{q},z) e^{i\mathbf{q}\cdot\mathbf{r}} | \psi_{l\mathbf{k}} \rangle
\end{aligned} \tag{27}$$

In Eq. 27, we assume the $|\mathbf{q}|$ is small and thus we use $W_{l'l}(\mathbf{q})$ (see Appendix B for how to calculate

from QEH model) to approximate $\langle \psi_{l\mathbf{k}+\mathbf{q}} | W_{l'}(\mathbf{q},z)e^{i\mathbf{q}\cdot\mathbf{r}} | \psi_{l\mathbf{k}} \rangle$. The $\bar{g}^{\mathrm{F}}$ can be evaluated as:

$$\bar{g}_{l\mu}^{\mathrm{F}}(\mathbf{k},\mathbf{q}) = \sum_{l'v} \frac{\tilde{e}_{\mathbf{q}\mu;l'v}}{\sqrt{2\tilde{\omega}_{\mathbf{q}\mu}}} \frac{ie^2}{A_{l'}} \frac{1}{\sqrt{N_{l'}}} |\mathbf{q}| W_{l'l}(\mathbf{q})z_{l'v} \tag{28}$$

Note that the $\bar{g}^{\mathrm{F}}$ definition in Eq. 23 leads to $\bar{g}^{\mathrm{F}}$ depending on BvK boundary conditions: i.e., the

$\bar{g}^{\mathrm{F}}$ in Eq. 28 is determined by $N_{l'}$. In realistic calculations, we prefer to eliminate the arbitrary N_l in

$\bar{g}^{\mathrm{F}}$. In the following, we show how to define a new $g_{l\mu}^{\mathrm{F}}$ that is independent to N_l. First we note that

the scattering rates should be a well-defined observables:

$$\frac{1}{\tau_{l\mathbf{k}}} = \sum_{\mathbf{k}'\in K_l} S(\mathbf{k},\mathbf{k}')$$
$$= \sum_{\mathbf{k}'\in K_l} \sum_{\mu} \frac{2\pi}{\hbar} |\bar{g}_{l\mu}^{\mathrm{F}}(\mathbf{k},\mathbf{k}'-\mathbf{k})|^2 \, w(\mathbf{k},\mathbf{k}') \tag{29}$$

where $S(\mathbf{k},\mathbf{k}')$ is the transition rate from initial state $\mathbf{k}$ to final state $\mathbf{k}'$, K_l is the set of reciprocal lattice grid. In Eq. 29, we use an integral on Brillouin zone to substitute the summation on final state $\mathbf{k}'$. This leads to:

$$\frac{1}{\tau_{l\mathbf{k}}} = N_l \int_l \frac{d\mathbf{k}'}{A_{l,\mathrm{BZ}}} \sum_{\mu} \frac{2\pi}{\hbar} |\bar{g}_{l\mu}^{\mathrm{F}}(\mathbf{k},\mathbf{k}'-\mathbf{k})|^2 \, w(\mathbf{k},\mathbf{k}')$$
$$= \int_l \frac{d\mathbf{k}'}{A_{l,\mathrm{BZ}}} \sum_{\mu} \frac{2\pi}{\hbar} |\sum_{l'v} \frac{\tilde{e}_{\mathbf{q}\mu;l'v}}{\sqrt{2\tilde{\omega}_{\mathbf{q}\mu}}} \frac{ie^2}{A_{l'}} \frac{\sqrt{N_l}}{\sqrt{N_{l'}}} |\mathbf{q}| W_{l'l}(\mathbf{q})z_{l'v}|^2 \, w(\mathbf{k},\mathbf{k}') \tag{30}$$
$$= \int_l \frac{d\mathbf{k}'}{A_{l,\mathrm{BZ}}} \sum_{\mu} \frac{2\pi}{\hbar} |\sum_{l'v} \frac{\tilde{e}_{\mathbf{q}\mu;l'v}}{\sqrt{2\tilde{\omega}_{\mathbf{q}\mu}}} \frac{ie^2}{\sqrt{A_l A_{l'}}} |\mathbf{q}| W_{l'l}(\mathbf{q})z_{l'v}|^2 \, w(\mathbf{k},\mathbf{k}')$$

where the property of BvK boundary condition $A_l N_l = A_{l'} N_{l'}$ is used. The Eq. 30 can be simply written as:

$$\frac{1}{\tau_{l\mathbf{k}}} = \int_l \frac{d\mathbf{k}'}{A_{l,\mathrm{BZ}}} \sum_{\mu} \frac{2\pi}{\hbar} |g_{l\mu}^{\mathrm{F}}(\mathbf{k},\mathbf{q})|^2 \, w(\mathbf{k},\mathbf{k}') \tag{31}$$

where $g_{l\mu}^{\mathrm{F}}(\mathbf{k},\mathbf{q})$ is:

$$g_{l\mu}^{\mathrm{F}}(\mathbf{k},\mathbf{q}) = \sum_{l'v} \frac{\tilde{e}_{\mathbf{q}\mu;l'v}}{\sqrt{2\tilde{\omega}_{\mathbf{q}\mu}}} \frac{ie^2}{\sqrt{A_l A_{l'}}} |\mathbf{q}| W_{l'l}(\mathbf{q})z_{l'v} \tag{32}$$

The Eq. 32 is the calculation equation of Fröhlich coupling (Eq. 9 in the main text) and the corresponding scattering rate can be obtained by Eq. 31.

Appendix B: Dielectric properties from QEH model

In Appendix A, we used screened potential matrix $W_{ll'}(\mathbf{q})$ to accurately describe the dielectric screening in vdW heterostructure, both in dynamical matrix (Eq. 19) and Fröhlich coupling matrix (Eq. 32). The screened potential matrix $W_{ll'}(\mathbf{q})$ quantifies the screened potential at layer l' induced by bare charge at layer l:

$$W = \epsilon^{-1} V \tag{33}$$

where ϵ^{-1} is the inverse dielectric function and V is the Coulomb kernel. In QEH model, the ϵ^{-1} and V are calculated using a mixed density/potential basis [3]:

$$\epsilon^{-1}_{l\alpha,l'\alpha'} = \langle \rho_{l\alpha} | \epsilon^{-1} | \phi_{l'\alpha'} \rangle$$
$$V_{l\alpha,l'\alpha'} = \langle \rho_{l\alpha} | V | \rho_{l'\alpha'} \rangle \tag{34}$$

where l, l' are layer indices in the vdW heterostructure, α, α' refer to monopole and dipole basis. (The definition of density/potential basis can be found in Eqs. 13-15 and 18 in Supporting Information of Ref. [3]) Here we are interested in Fröhlich scattering which only involves in-plane lattice vibration and "monopole" like charge distribution. So we omit the α subscript in Eq. 34 in the following. Using the same basis, the W in Eq. 33 can be calculated via QEH model by:

$$W_{ll'}(\mathbf{q}) = \langle \rho_{l'} | W | \rho_l \rangle = \sum_k \epsilon^{-1}_{l'k}(\mathbf{q}) V_{kl}(\mathbf{q}) \tag{35}$$

where ϵ^{-1} and V matrix can be obtained from QEH code. The screened interaction $\bar{W}_{ll'}$ used in dynamical matrix is defined as:

$$\bar{W}_{ll'}(\mathbf{q}) = \frac{W_{ll'}(\mathbf{q}) + W_{l'l}(\mathbf{q})}{2} \tag{36}$$

When $l=l'$, the $W_{ll'}$ can be approximated by [6]:

$$W_{ll}(\mathbf{q}) = \frac{2\pi}{|\mathbf{q}|(1 + 2\pi\alpha^{\|}|\mathbf{q}|)} \tag{37}$$

for isotropic 2D materials, where $\alpha^{\|}$ is the in-plane polarizability. Based on Eq. 19 or Ref. [6], the POP frequency for individual layer l with $W_{ll}(\mathbf{q})$ from Eq. 37 has:

$$\omega^2_{\mathbf{q}lv} = \omega^2_{0lv} + \frac{e^2 z^2_{lv}}{A_l} \frac{2\pi |\mathbf{q}|}{1 + 2\pi\alpha^{\|}|\mathbf{q}|} \tag{38}$$

Therefore, for large $|\mathbf{q}|$, from Eq. 38 we have:

$$\omega^2_{\mathbf{q}\to\infty,lv} = \omega^2_{0lv} + \Delta\omega^2_{lv} \tag{39}$$

where $\Delta\omega$ is Eq. 12 in the main text:

$$\Delta\omega_{POP} = \frac{e z_{POP}}{\sqrt{\alpha^{\|} A}} \tag{40}$$

From Eq. 39 we can see the $\Delta\omega$ is indeed the frequency increase of POP, verifying the statement below Eq. 12 in the main text.

Appendix C: Model verification from first principles

In this section, we use the first-principles approach to verify our Fröhlich heterostructure model. A heterostructure ZrS_2/HfS_2 is constructed and Density functional perturbation theory (DFPT) calculation is performed on this structure to obtain electron-phonon coupling g matrix and phonon frequency of whole structure. The ZrS_2 and HfS_2 are selected due to their close lattice constants and large Born effective charges, which ensures large POP couplings between two layers. In practice, the first-principles calculations are performed using the Quantum Espresso Package [7,8] with SG15 Optimized Norm-Conserving Vanderbilt (ONCV) pseudopotentials [9,10] and the Perdew-Burke-Ernzerhof (PBE) exchange-correlation functional [11]. The 2D Coulomb cutoff technique [12] is applied to avoid fictitious EPC between image charges in DFPT calculations [13].

Figure S1 shows the calculated EPC strengths and phonon frequency for selected optical phonon modes. In Figures S1 a and b, the EPC strengths in ZrS_2 from different calculation approaches: first-principles DFPT, model EPC without POP coupling (denoted as 'ph-isolated') and model EPC with POP coupling (denoted as 'ph-coupled') are compared. Since ZrS_2 and HfS_2 have anisotropic effective mass, here we compare the EPC with same initial state at CBM but with different final states along different directions, as diagramed in insets in figures. We can see for both directions, the full model EPC strengths (blue lines) are consistent with the DFPT benchmarks (red circles), especially for two coupled LO phonon modes (indicated by 'LO_1' and 'LO_2'), which verify the correctness and accuracy of our heterostructure Fröhlich model. We also show the model EPC strengths without POP coupling (orange dashed lines) originating two LO modes in two bilayers. As we can see, the EPC without POP coupling deviate from the correct trend, especially for LO_1 around $\mathbf{q}=0$. The direct comparison here proves that the LO coupling indeed reduce Fröhlich scattering for one LO mode while enhance another one. The Figures S1 c and d displayed similar trends of EPC for EPC in HfS_2. As last, the phonon frequency for all optical modes calculated from DFPT and our Fröhlich model are compared in Figure S1 e and f. As we can see, all optical modes show smooth dispersion at $\mathbf{q}$ scales considered around zone center except LO modes. In addition to EPC strengths, our model correctly captures the $\mathbf{q}$-dependence of LO mode frequency for both $\mathbf{q}$ directions.
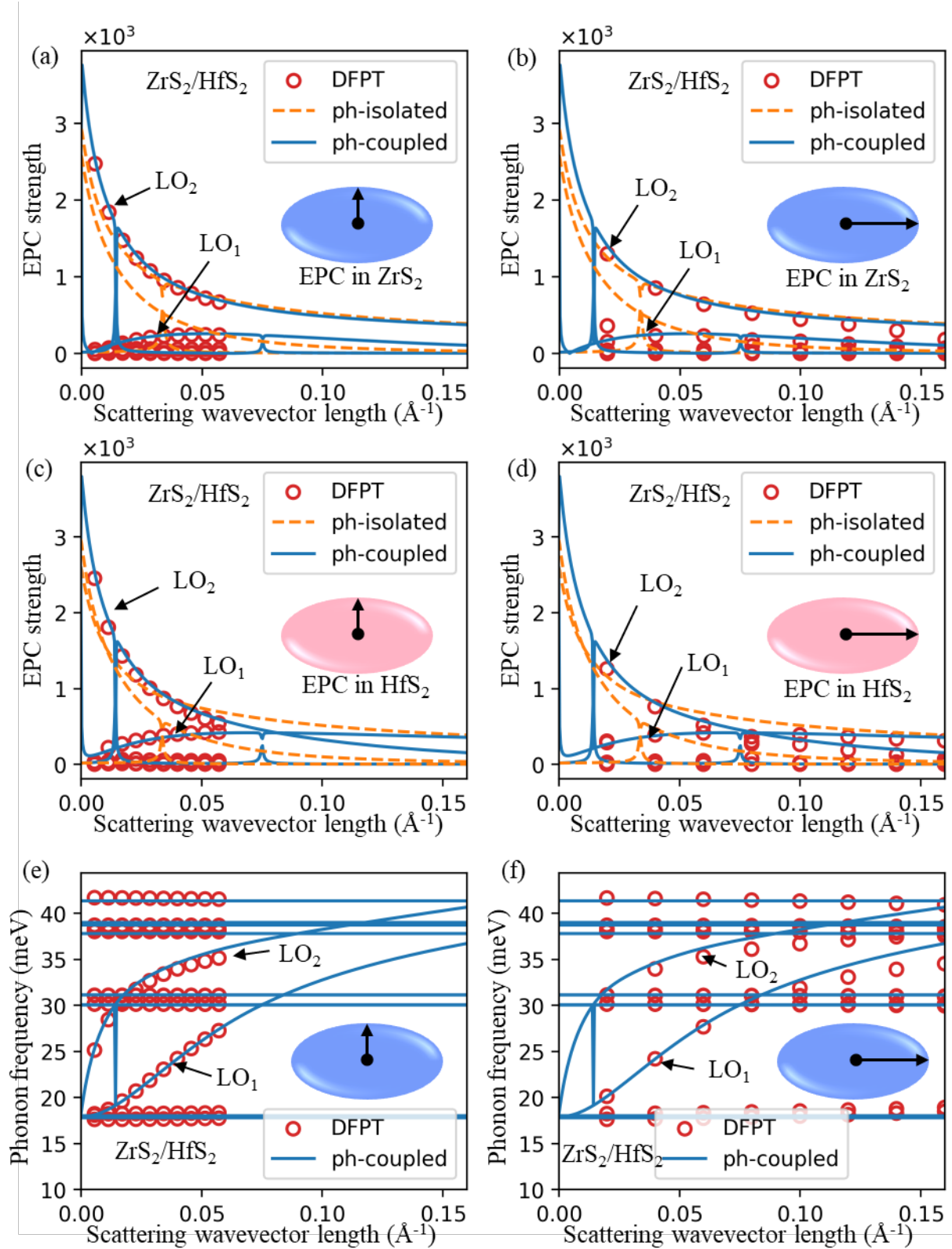
Figure S1 Electron phonon coupling strengths in ZrS_2 in bilayer heterostructure ZrS_2/HfS_2 calculated from first principles (DFPT), heterostructure Fröhlich model with ('ph-coupled') and without ('ph-isolated') POP coupling (see main text for definition) for phonon wavevector $\mathbf{q}$ along x (a) and y (b) directions. (c) and (d) are similar to (a) and (b) but for EPC strength in HfS_2. Phonon dispersion of ZrS_2/HfS_2 optical modes for $\mathbf{q}$ along x (e) and y (f) directions.

[1] S. Baroni, S. de Gironcoli, A. Dal Corso, and P. Giannozzi, Rev. Mod. Phys. **73**, 515 (2001).

[2] C. Verdi and F. Giustino, Phys. Rev. Lett. **115**, 176401 (2015).

[3] K. Andersen, S. Latini, and K. S. Thygesen, Nano Lett. **15**, 4616 (2015).

[4] M. N. Gjerding, L. S. R. Cavalcante, A. Chaves, and K. S. Thygesen, J. Phys. Chem. C **124**, 11609 (2020).

[5] F. Giustino, Rev. Mod. Phys. **89**, 015003 (2017).

[6] T. Sohier, M. Gibertini, M. Calandra, F. Mauri, and N. Marzari, Nano Lett. **17**, 3758 (2017).

[7] P. Giannozzi *et al.*, J. Phys.: Condens. Matter **21**, 395502 (2009).

[8] P. Giannozzi *et al.*, J. Phys.: Condens. Matter **29**, 465901 (2017).

[9] M. Schlipf and F. Gygi, Computer Physics Communications **196**, 36 (2015).

[10] D. R. Hamann, Phys. Rev. B **88** (2013).

[11] J. P. Perdew, K. Burke, and M. Ernzerhof, Phys Rev Lett **77**, 3865 (1996).

[12] T. Sohier, M. Calandra, and F. Mauri, Phys. Rev. B **96** (2017).

[13] P. Giannozzi, S. de Gironcoli, P. Pavone, and S. Baroni, Phys Rev B Condens Matter **43**, 7231 (1991).